(RESEARCH ARTICLE)

Check for updates

Multifractal structure of cholinergic innervation in the tunica albuginea of rat testis. Comparison with different models simulating nerve networks

Luis Santamaría [1, *] and Ildefonso Ingelmo [2]

[1] Department of Anatomy, Histology, and Neuroscience. School of Medicine, Autonomous University of Madrid. C/Arzobispo Morcillo 2, 28029-Madrid, Spain.
[2] Department of Anaesthesiology. Hospital Ramón y Cajal, Madrid, Spain.

Abstract

The complexity of the distribution of cholinergic innervation of the albuginea suggests that its structural pattern may exhibit multiple scaling rules rather than a single global scale. Therefore, the study of nerve fibers could be approached through multifractal analysis. The cholinergic fiber plexuses of the rat testicular albuginea, visualized by a histochemical technique for the detection of acetylcholine sterases, will be analyzed for the possible detection of their multifractal structure, calculating several types of multifractal spectra, namely multifractal spectrum f(α) versus α, and the generalized dimension DQ versus Q. In the present study, the results will be compared with the multifractal spectra of plexus models consisting of the elaboration of interconnected line lattices generated, either employing a binary matrix or using a tessellation matrix, and according to various realizations of randomly distributed points in a two-dimensional space. The results of this study suggest that the cholinergic nerve plexuses of the testicular albuginea of the rat show a multifractal behavior, and the multifractality of the real data is greater than that of the simulated networks. However, Voronoi tessellations models show a more remarkable similarity of the multifractal scale with the real data in comparison with those generated by a binary matrix.

Keywords: Testicular albuginea; Cholinergic plexuses; Multifractals; Generalized fractal dimension; Simulated networks; Voronoi tessellations

1 Introduction

The testicular albuginea of the rat has some small nerve bundles, mainly located near the testicular mediastinum, and isolated nerve endings that are irregularly distributed throughout its area [1]. However, according to various authors, the highest proportion of nerve fibers is arranged with blood vessels of the tunica vasculosa [1]. Some findings of histochemical features of cholinergic innervation of rat albuginea were described in a study by Reoyo et al. [2] and could be summarized as follows: The tunica adventitia of the testicular artery that runs across the albuginea from the superior to the inferior testicular poles was seen to contain a rich plexus of acetylcholinesterase positive nerve fibers. In the mediastinum testis, collateral branches of this plexus formed a broad network with fibers ending beneath the rete testis epithelium. In its course along the testicular artery, the plexus gave rise to many other branches extending laterally over the testis without reaching its ventral portion. In turn, these branches originated another series of fibers running parallel to the longest testicular axis towards either the testis' superior or inferior poles. In summary, the testicular albuginea of the rat has an important plexus of cholinergic nerve fibers with a marked directional component following the testicular long axis. The length density, the absolute length of these fibers, and the degree of preferential orientation in a spatial direction (anisotropy) have already been studied [3]. However, the complexity of nerve ramifications and their possible fractal structure have not been addressed yet. As with other biological textures [4-7], the complexity of branching and distribution of nerve fibers in the testicular albuginea could be characterized by fractal geometry, and such geometry could be related to a nonlinear deterministic dynamic underlying the processes of neurogenesis. In

* Corresponding author: Luis Santamaría ORCID: 0000-0001-6560-2502

addition, the complexity of the distribution of nerve fibers likely extends through different scales since there are different sizes and orders of branching; therefore, it is likely that the fractal dimension is not unique but that we are dealing with a multifractal structure [8, 9]. Recently, many physical quantities that do not obey conventional scaling laws have been considered. Broad probability distributions are characteristic of such observables. In all cases, the moments of the distributions cannot be characterized by a single exponent. An infinity hierarchy of exponents is required. This phenomenon was described for the first time by B. B. Mandelbrot in the context of fully developed turbulence [10]; today, it is known by the neologism multifractality.

The fractal dimension is the basic notion for describing structures with a scaling symmetry. Scaling symmetry means self-similarity of the considered object on varying scales of magnification. Therefore, a fractal dimension is an index for characterizing fractal patterns by quantifying their complexity as a ratio of the change in detail to the change in scale [11]. Briefly, three types of fractal dimension can be defined, depending on the methodology used for their estimation and the aspect of fractality on which they emphasize:

- The fractal dimension by box counting (D_B), often identified with the Hausdorff dimension, is the absolute value of the slope of the regression line represented in a log-log plot between the size of the box (scale) and the number of boxes occupied by pixels of the scanned structure. According to multifractal terminology [12], D_B is equivalent to D_0, where D_0 is the fractal dimension for the moment Q = 0, also called the capacity dimension.
- The Information dimension, D_1, considers how the average information needed to identify an occupied box scales with box size, where *p* is the probability of finding a point of the fractal in the i-th cube of size ε;

$$D_1 = \lim_{\varepsilon \to 0} \frac{-\langle \log p_\varepsilon \rangle}{\log 1/\varepsilon}$$

- The correlation dimension, D_2, is a fractal dimension [13-16] and represents the probability that two points in the phase space are separated by Euclidean distance less than or equal to r [17]. The correlation dimension represents a characteristic of the attractor's geometry. It is related to the mode of distribution of its points in the space so that the more complex and folded the orbits of the attractor are, the greater will D_2. In general, all these dimensions are different for one fractal object. Only in the case of the well-known simple fractals, monofractals, a single dimension suffices, and $D_0 = D_1 = D_2$. Nevertheless, a "unique fingerprint" of a multifractal object requires the introduction of an infinite hierarchy of fractal dimensions [18-21]. Monofractal signals are homogeneous because they have the same scaling properties throughout the entire signal. In contrast, multifractals are structures that have multiple scaling rules instead of a single global scale [9, 11]. Monofractals can be indexed by a global Hölder exponent [22]; this is an exponent that shows how irregular the function is [23]. At the same time, multifractal signals can be decomposed into many subsets characterized by different local Hölder exponents, which quantify local and singular behavior and are related to the local scaling of the temporal (or spatial) series. Thus, multifractal signals require many exponents to characterize their scaling properties completely [24].

The complexity of the distribution of cholinergic innervation of the albuginea suggests that its structural pattern may exhibit multiple scaling rules rather than a single global scale. That is, the study of nerve fibers could be approached through multifractal analysis. Therefore, in the present work, the cholinergic fiber plexuses of the rat testicular albuginea, visualized by a histochemical technique for the detection of acetylcholinesterases, will be analyzed for the possible detection of their multifractal structure, calculating several types of multifractal spectra.

Models of realizations of point processes (Poisson type and others) associated with Voronoi-Delaunay tessellations have been applied to simulate different biological structures and their possible functional correlates, such as cellular interactions [25] distribution of renal glomeruli in normal and pathological mice [26] structure and distribution of pulmonary acini [27], nerve cell patterning [28], etc., in the present study the results will be compared with the multifractal spectra of plexuses models consisting of the elaboration of interconnected line lattices according to various realizations of randomly distributed points in a two-dimensional space [25].

2   Material and methods

Five male Wistar rats, weighing an average of 250 g, were killed by carbon dioxide inhalation. The rats were bred and manipulated following the bioethical standards of international organizations (WMA Statement on Animal Use in Biomedical Research), European Union guidelines, and Spanish State and Local regulations for the use of animals in research, and approved by the Ethical and Animal Studies Committee of the Autonomous University of Madrid. After

euthanizing the animals, a longitudinal incision was made in both scrotal pouches, and the testes and epididymis were removed, sectioning at the level of the lower third of the spermatic cord. The testis was freed from the paratesticular structures, and the subepididymal adipose tissue pads were removed; then, a longitudinal incision (2-3 mm in length) was made over the entire anterior border of the testicle from the upper to the lower pole. Next, the testicular parenchyma was carefully extracted, avoiding possible lesions of the testicular artery and the tunica vasculosa. Four additional incisions were made obliquely to the tissue's long axis (two in the upper pole and two in the lower pole) to facilitate the complete extension of the albuginea in one plane. The albuginea, thus isolated, was washed with cold isotonic serum. The albuginea was then spread on a flat silicon surface where it was fixed, constantly moistening in isotonic saline. Once the albuginea was obtained, a histochemical technique was used to visualize the cholinergic fibers *in toto* preparations (whole mount technique), as other authors [29, 30] have done to study the innervation of the blood vessels. In the present study, the Karnovsky-Roots technique was used; briefly: the tissue was incubated for 40-60 minutes at room temperature in the Karnovsky-Roots medium that uses acetyl-thiocholine iodide as substrate [31-36], modified by EI-Badawi [37]. The incubation process is monitored under the microscope, stopping when the nerve plexuses' satisfactory staining is observed (approximately 2 hours). The extended albuginea is then mounted on a slide. The preparation is treated with 1% osmium tetroxide. It is washed in distilled water in five changes of 3 minutes each. The non-specific activity of cholinesterases was inhibited by adding iso-OMPA, 4 mM, to the medium [38, 39]. After incubation, the tissue was washed in phosphate-buffered saline at pH 7.2, dehydrated in ethanol, and mounted in a synthetic resin (Depex, Serva, Heidelberg, Germany). The albuginea specimens mounted on slides were examined using an Olympus microscope fitted with a motorized stage controlled by Cast-Grid's stereological software (Stereology Software Package, Silkeborg, Denmark); this program monitors the XY displacement of the microscope stage. At low magnification (x4), the total area covered by the albuginea was selected, and using the software's sampling system (meander sampling), an average of 10 fields was chosen with a uniform random distribution throughout the entire tissue extension. In each selected field, a total of 10 images were acquired at a magnification of x4 (at that magnification, 512 pixels correspond to 262 μm); each specimen collection of 10 images was stored in jpeg format and processed for its binarization with Image J software (version 1.48), developed at the US National Institutes of Health and available on the Internet at *https://imagej.nih.gov/ij/index.html* [40]. The software for the estimation of multifractal parameters included in the FracLac plugging from Image J software (version 1.48) was applied in all of the binarized images from each case studied. FracLac generates a mass distribution for a binarized image; from this, a spectrum of values for the generalized dimension (D_Q) is calculated. D_Q addresses how mass varies with an image's ε (resolution or box size). The multifractal analysis applies a distorting factor to datasets extracted from patterns to compare how the data behave at each distortion. This is done using graphs known as multifractal spectra, analogous to viewing the dataset through a"distorting lens". One practical multifractal spectrum is the graph of D_Q vs Q, where D_Q is the generalized dimension for a dataset, and Q is an arbitrary set of exponents. The expression generalized dimension thus refers to a set of dimensions for a dataset. The general pattern of the graph of D_Q vs Q can be used to assess the scaling in a pattern. The graph generally decreases and is sigmoidal around Q = 0, where $D_0 \geq D_1 \geq D_2$. The generalized dimension also gives important specific information. D_0 is equal to the capacity dimension (box counting dimension). D_1 is equal to the information dimension, and D_2 is equal to the correlation dimension. Multifractals have multiple dimensions in the D_Q versus Q spectra, but monofractals stay relatively flat in that area.

Another useful multifractal spectrum is the f(α) graph over a range of diverging exponents α.

$$\alpha_i = \frac{\log \frac{m_{[i,\varepsilon]}}{M_\varepsilon}}{\log \varepsilon^{-1}}$$

Where:
i = index for each box over the set for a scale ε
$m_{[i,\varepsilon]}$ = number of pixels on the box i at scale ε
M_ε = total pixels in all boxes for the scale ε

$$f(\alpha) = \alpha \times Q - \left(D_Q \times (Q - 1) \right)$$

Where:
Q = the arbitrary set of exponents used for calculating spectra
D_Q = generalized dimension for the data set

This graph generally rises to a maximum approximating the fractal dimension at Q=0 and then falls. Like D_Q versus Q spectra, f(α) shows typical patterns for comparing non-, mono-, and multifractal patterns. In particular, non- and mono-

fractals converge on specific values for this spectrum, whereas the spectrum from multifractal patterns typically forms humps over a broader area. FracLac delivers the multifractal measures and graphs the typical multifractal spectra of $f(\alpha)$ versus α and D_Q versus Q.

In summary, on the binarized images, the following estimates were performed:

- Multifractal spectrum $f(\alpha)$ versus α.
- In the graph $f(\alpha)$ vs α the divergence was estimated. This is a measure of multifractality, also called Green divergence (ρ) [7]. Divergence is based on the minimum and maximum values for the $f(\alpha)$ versus α for the two sets of values around each side of $Q = 0$. Mathematically, it is the ratio of the areas defined by the spectra within those two spaces multiplied by 100, calculated in the space defined by the Qset used in determining the multifractal spectra; the greater the value of ρ, the greater multifractality the data set will possess.

$$\rho = \frac{(\alpha_0 - \alpha_{min}) \times (f(\alpha_0) - f(\alpha_{min}))}{(\alpha_{max} - \alpha_0) \times (f(\alpha_0) - f(\alpha_{max}))} \times 100$$

Where α_0 is the alpha exponent at $Q = 0$, α_{min} is the alpha exponent at minimum value of Q, and α_{max} is the alpha at maximum value of Q, in the range of values of Q used.

- Generalized dimension D_Q versus Q.
- From the D_Q vs Q graph, the dimensions D_0 (capacity dimension), D_1 (information dimension), and D_2 (correlation dimension) were extracted.

Each value of Q is an exponent used in calculating the multifractal spectra. The maximum, minimum, and increment between Qs are arbitrary values the user sets; the range employed was from -10 to 10, incremented by 0.1.

All these measurements were carried out on each case's images, obtaining at the end graphs in which the mean of each estimator ± CI (95%) was expressed.

In order to compare the multifractal spectra of the real data, a statistical software package in R (spatstat) was employed [41, 42] for the elaboration of some models of the nerve plexuses. The protocol was as follows:

-Five simulations of point processes were carried out:

- Rpoispp: Generates a random point pattern using the Poisson process and includes CSR (complete spatial randomness).
- Rssi: This algorithm generates a realization of the Simple Sequential Inhibition point process. Starting with an empty window, the algorithm adds points one by one. Each new point is generated uniformly in the window and independently of preceding points. If the new point lies closer than r units from an existing point, it is rejected, generating another random point.
- Runifpoint: This function generates n independent random points, uniformly distributed.
- Rmatclust: This algorithm generates a realization of Matern's cluster process. The process is constructed by first generating a Poisson point process of "parent" points with intensity κ. Then, each parent point is replaced by a random cluster of points, the number of points in each cluster being random with a Poisson distribution, and the points being placed independently and uniformly inside a disc of radius r centered on the parent point.
- Rsyst: Generates a "systematic random" pattern of points in a window, consisting of a grid of equally-spaced points with a random common displacement.

For each simulation, a set of pairs of coordinates (points) was obtained; the average number of coordinate pairs was 26 per image, and the size of each image was 742 x 1024 pixels (379 x 523 μm).

From each set of coordinates, in each simulation, two different types of network of connections were built using segments following the Delaunay tessellation method: a binary connection matrix and the tessellation matrix [43]. The networks generated using the points processes above indicated are expressed in Table 1, and some examples of the realizations of points and the different types of generated networks (Figures 1,2) are displayed.

Table 1 Networks generated using diverse point realizations

Point realizations[1]	Network type 1[2]	Network type 2[3]
Rpoispp	poiss1	poiss2
Rssi	ssi1	ssi2
Runifpoint	unif1	unif2
Rmatclust	matclust1	matclust2
Rsyst	syst1	syst2

[1]Simulations of point processes used as nodes to interconnect linear segments. [2]Networks generated by segments produced by a binary matrix. [3]Networks generated by segments produced by a tessellation matrix.
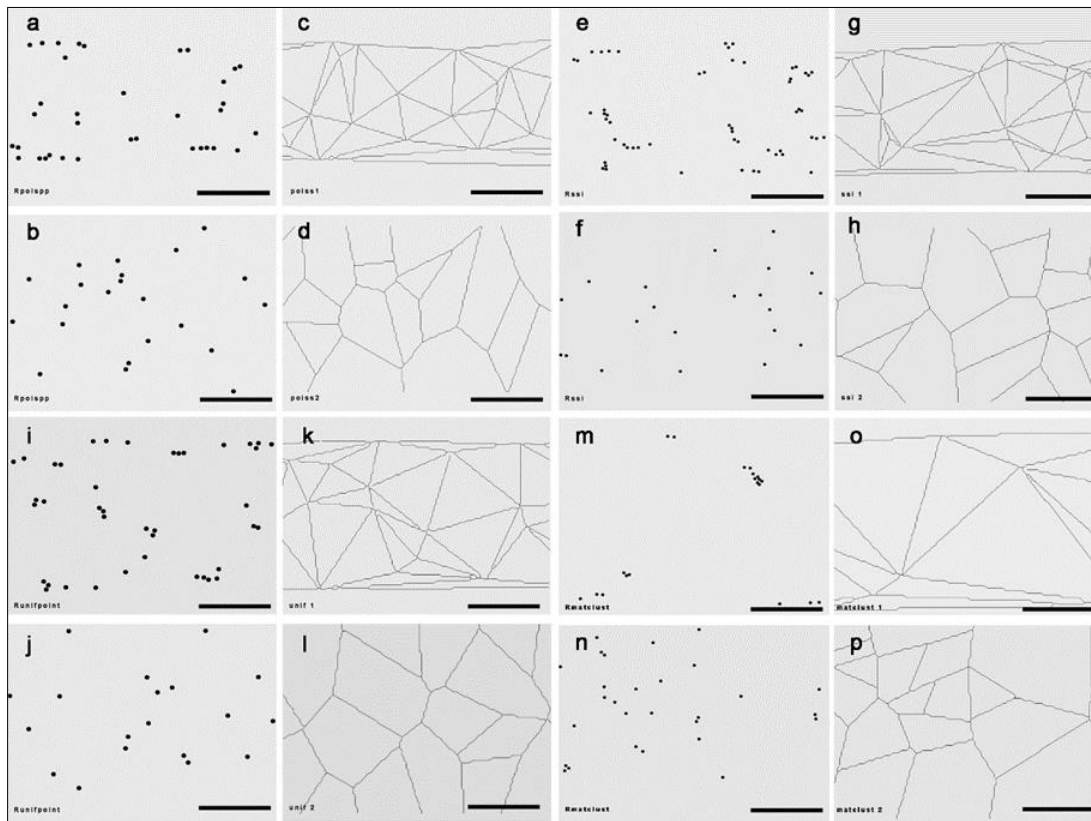

Figure 1 a, b: Images showing random point patterns generated by a Poisson process (Rpoispp). c: Image of a network of segments obtained from Rpoispp points using a binary matrix (poiss1). d: Image of a network of segments obtained from Rpoispp points using a tessellation matrix (poiss 2). e,f: Images showing random point patterns generated by a realization of the simple sequential inhibition point process (Rssi). g: Image of a network of segments obtained from Rssi points using a binary matrix (ssi 1), h: Image of a network of segments obtained from Rssi points using a tessellation matrix (ssi 2). i, j: Images showing point patterns generated by independent random points, uniformly distributed (Runifpoint). k: Image of a network of segments obtained from Runifpoint using a binary matrix (unif 1). l: Image of a network of segments obtained from Runifpoint using a tessellation matrix (unif 2). m,n: Images showing random point patterns generated by a realization of Matern's cluster process (Rmatclust). o: Image of a network of segments obtained from Rmatclust using a binary matrix (matclust 1). p: Image of a network of segments obtained from Rmatclust using a tessellation matrix (matclust 2). The scale bars represent 580 μm

Five different realizations were carried out for each point process so that five type 1 networks and another five type 2 networks have been obtained for each point process. Next, the mean of the multifractal parameters for each realization ± SEM was obtained to compare with the real data. Comparisons between the means from ρ, and D_0, D_1, and D_2 for real

and simulated network groups were performed by ANOVA (p < 0.05). The multifractal spectra f(α) vs α and D_Q vs Q were represented graphically using Prism 7.00 (Graph-Pad Software).
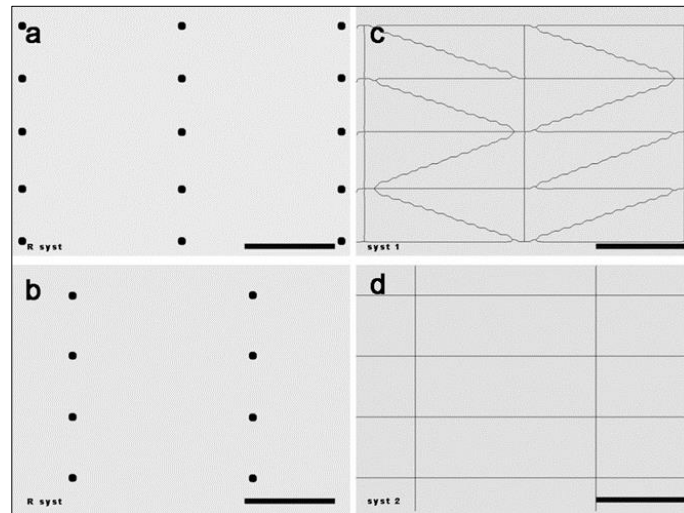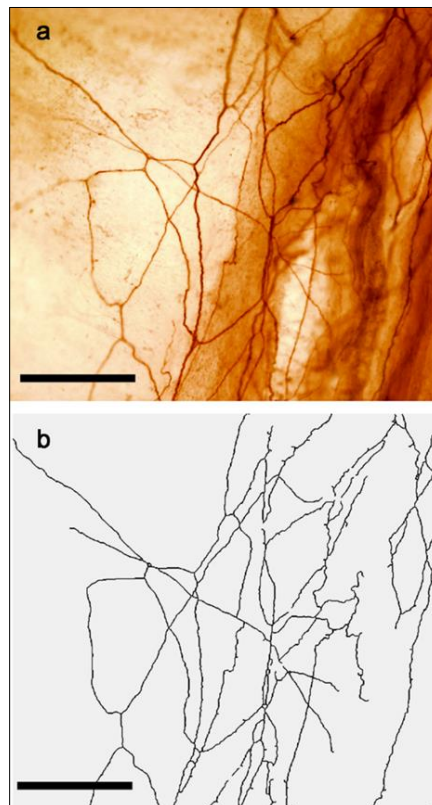

Figure 2 a, b: Images showing a systematic random pattern of points (Rsyst). c: Image of a network of segments obtained from Rsyst points using a binary matrix (syst 1). d: Image of a network of segments obtained from Rsyst points using a tessellation matrix (syst 2). The scale bars represent 580 µm

3   Results

Figure 3 a Whole mount of the testicular albuginea of the rat stained to show the plexuses of cholinergic innervation. b: The image from (a) was processed to segment the stained nerve fibers; subsequently, the image was binarized and skeletonized. The scale bars represent 580 µm

The tunica adventitia of the testicular artery that runs across the albuginea from the superior to the inferior testicular poles contained a rich plexus of acetylcholinesterase-positive (AchE) nerve fibers. Collateral branches of this plexus are observed developing a broad network with fibers ending beneath the rete testis epithelium (Figure 3 a,b).

3.1   Multifractal spectra f(α) vs α

The multifractal spectrum of the AchE positive plexuses of the testicular albuginea shows a humped morphology with the branch of the graph of α values for Q ≤ 0 longer than that of the corresponding values for the range of values for Q ≥ 0, the maximum value of α (Q = 0) is 1.45 (Figures 4, 5). When the spectrum of the real data is compared with the spectra obtained for the different networks generated by segments produced by a binary matrix, it is observed that the curve of the models moves to the left of the graph; this displacement was significant for the branch of α values in the range of Q ≥ 0 (Figures 4, 5).
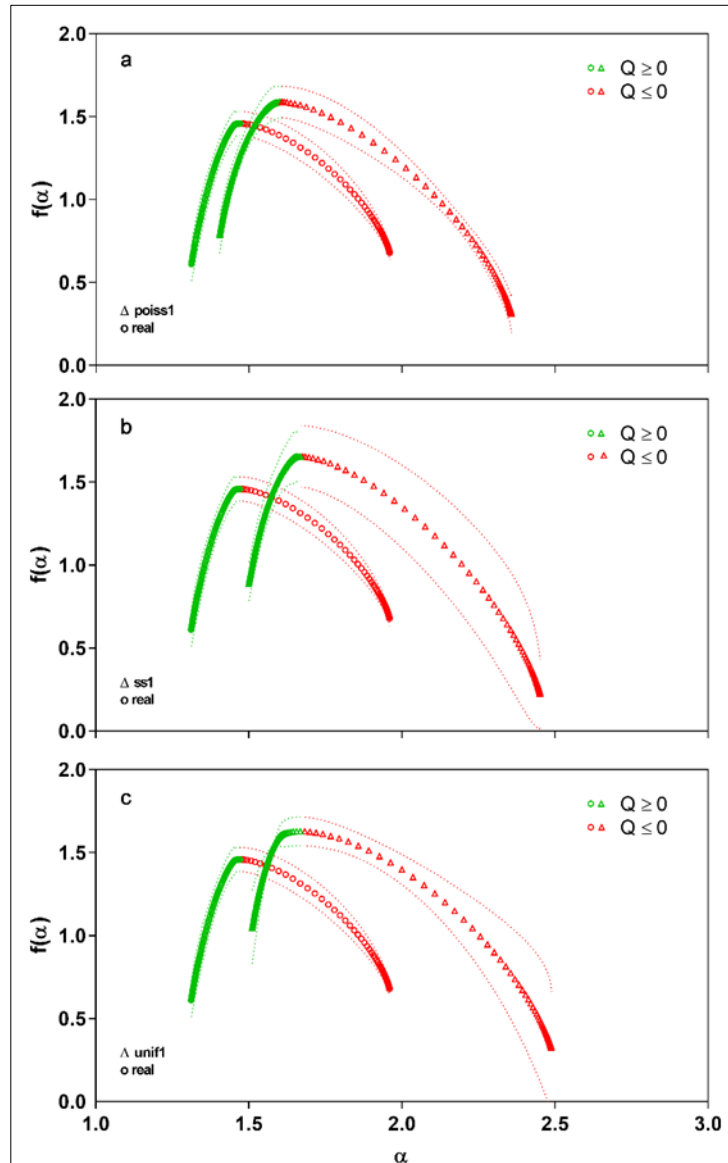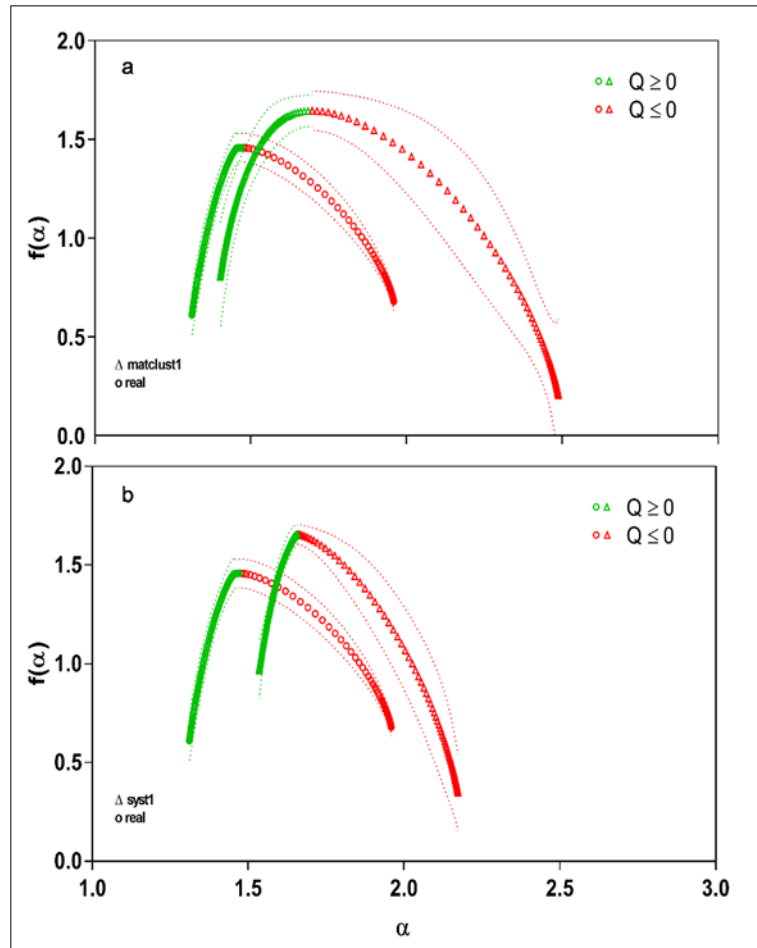

Figure 4 Multifractal spectrum f(α) of the cholinergic fiber plexus of the rat testicular albuginea (real) in comparison with the network models: poiss 1 (a), ss1 (b), and unif 1 (c). The values of the diverging exponent α are expressed on the ordinate axis, and the values of f(α) are expressed on the abscissa axis. The branch of the curves for the range of Q ≥ 0 is indicated in green, and the branch for Q ≤ 0 in red. The dotted lines for each curve express the 95% confidence intervals (CI)

Figure 5 Multifractal spectrum f(α) of the cholinergic fiber plexus of the rat testicular albuginea (real) in comparison with the network models: matclust 1 (a) and syst 1 (b). The values of the diverging exponent α are expressed on the ordinate axis, and the values of f(α) are expressed on the abscissa axis. The branch of the curves for the range of Q ≥ 0 is indicated in green and the branch for Q ≤ 0 in red. The dotted lines for each curve express the 95% confidence intervals (CI)

The model that shows the least displacement is matclust1 (Figure 5a). When the alpha spectrum for the real values is compared with that of the networks generated by segments produced by a tessellation matrix, the overlapping of the branch of real α values for Q ≥ 0 with the simulated ones is visualized in all cases (Figures 6,7).

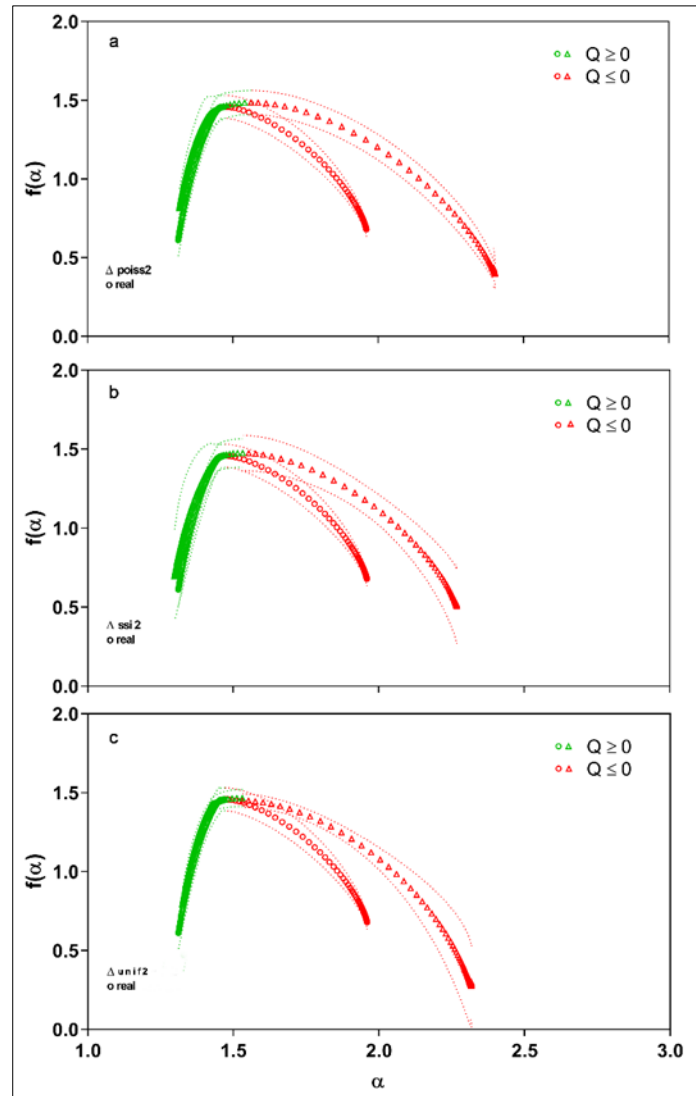**Figure 6** Multifractal spectrum f(α) of the cholinergic fiber plexus of the rat testicular albuginea (real) in comparison with the network models: poiss 2 (a), ss2 (b), and unif 2 (c). The values of the diverging exponent α are expressed on the ordinate axis, and the values of f(α) are expressed on the abscissa axis. The branch of the curves for the range of Q ≥ 0 is indicated in green, and the branch for Q ≤ 0 in red. The dotted lines for each curve express the 95% confidence intervals (CI)
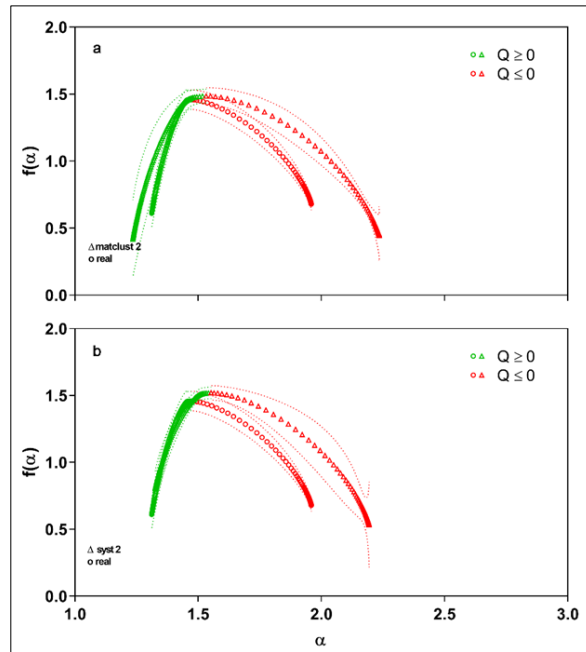
Figure 7 Multifractal spectrum f(α) of the cholinergic fiber plexus of the rat testicular albuginea (real) in comparison with the network models: matclust 2 (a) and syst 2 (b). The values of the diverging exponent α are expressed on the ordinate axis, and the values of f(α) are expressed on the abscissa axis. The branch of the curves for the range of Q ≥ 0 is indicated in green, and the branch for Q ≤ 0 in red. The dotted lines for each curve express the 95% confidence intervals (CI)

The divergence estimate (ρ) shows that when ρ of the real data is compared with the same measure of the models built from a binary matrix, the real ρ is significantly higher in all cases (Figure 8a). However, ρ does not show significant differences between the real and simulated data when generated from a tessellation matrix, except for the unif 2 network, which shows significantly less divergence than the real data (Figure 8b).
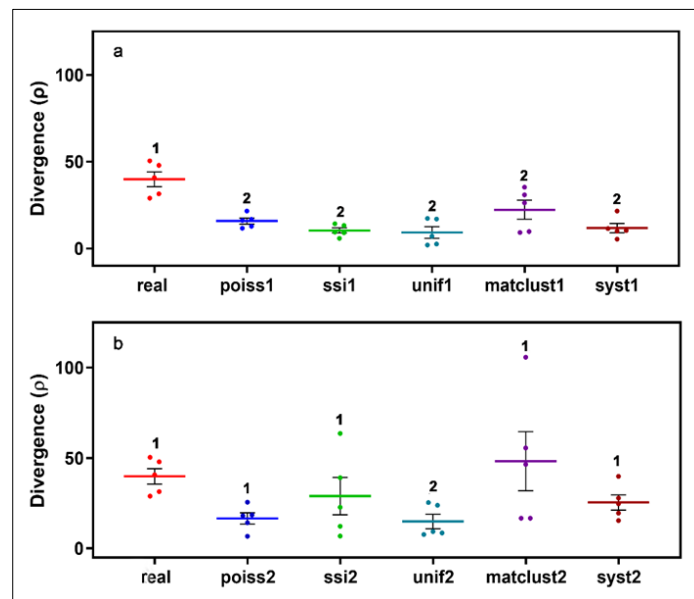

Figure 8 a: Scatter dots of the divergence (ρ) of the real data compared to the network models obtained from a binary matrix. b: Scatter dots of the divergence (ρ) of the real data compared to the network models obtained from a tessellation matrix. In both images, the dots indicate the individual cases of each group, the horizontal lines represent the mean, and the error bars indicate the SEM. Numbers placed above each error bar show significance: Error bars affected by different numbers indicate significant differences of simulated data compared to real data. Error bars affected by equal numbers indicate non-significant differences between those groups

3.2 Generalized dimension D_Q vs Q

When the curve of the D_Q vs Q of the real data is compared with the curves of the models generated from a binary matrix, the branch of the curve of the real data is significantly below the same branch of the simulated data for the range of values $Q \leq 0$ (Figure 9 a-c; and Figure 10 a,b). However, the branch of the D_Q vs Q curve of the real data for the range of values $Q \geq 0$ approximates the curves of the simulated data, the differences being significant only with the simulations unif1 and syst1 (Figure 9c and Figure 10b).
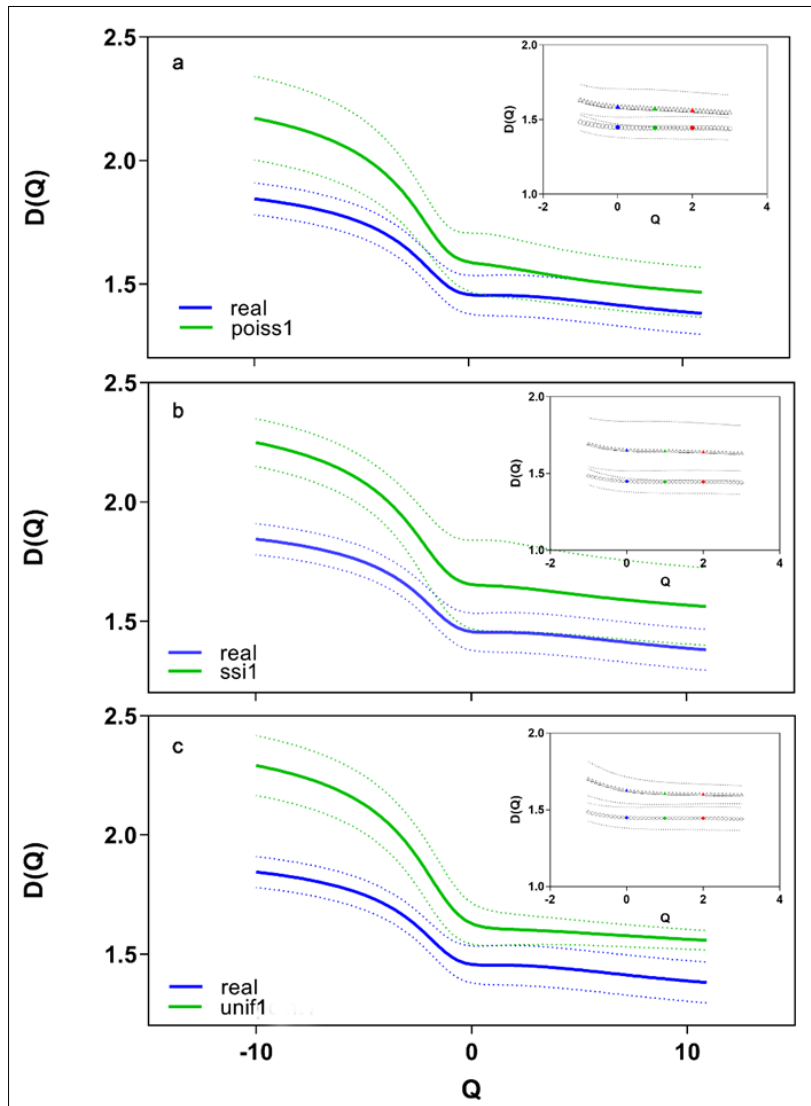

Figure 9 Graphs of the generalized dimension D(Q) as a function of Q. Q values are represented on the X axis, and D(Q) is on the Y axis. a: D(Q) obtained for the cholinergic innervation of the testicular albuginea of the rat (real data) is compared with D(Q) for the poiss 1 network; b: D(Q) of the real data is compared to D(Q) for the ssi1 network; c: D(Q) of the real data is compared to D(Q) for the unif1 network. All these networks have been generated by using a binary matrix. The insets of each graph show the section of the curve between Q = 0 and Q = 2 to show the dimension of capacity Q_0 (blue), information Q_1 (green), and correlation Q_2 (red). The dotted lines for each curve express the 95% confidence intervals (CI)
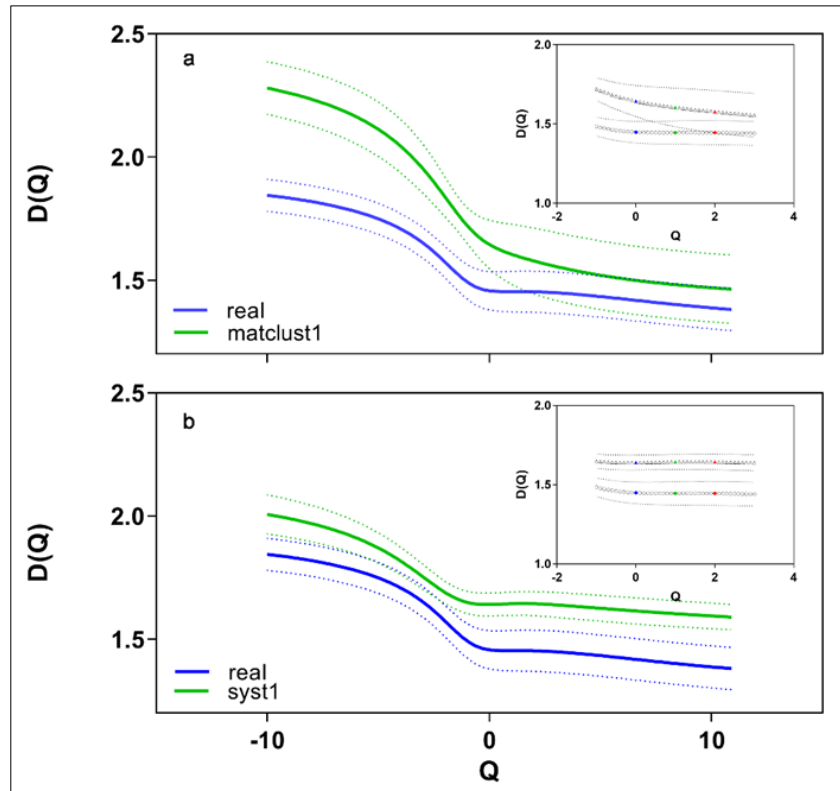
Figure 10 Graphs of the generalized dimension D(Q) as a function of Q. Q values are represented on the X axis, and D(Q) is on the Y axis. a: D(Q) obtained for the cholinergic innervation of the testicular albuginea of the rat (real data) is compared with D(Q) for the matclust1 network; b: D(Q) of the real data is compared to D(Q) for the syst 1 network. All these networks have been generated by using a binary matrix. The insets of each graph show the section of the curve between Q = 0 and Q = 2 to show the dimension of capacity Q_0 (blue), information Q_1 (green), and correlation Q_2 (red). The dotted lines for each curve express the 95% confidence intervals (CI)

When the D_Q vs Q curve for the real data is compared to the simulation curves obtained from a tessellation matrix, the branch of the real data curve for the range of Q ≤ 0 is significantly below the same branch of the curve in all generated simulations. However, the branch of the curve of the real data in the range Q ≥ 0 does not differ significantly from all the simulations produced (Figure 11 a-c; and Figure 12 a,b).
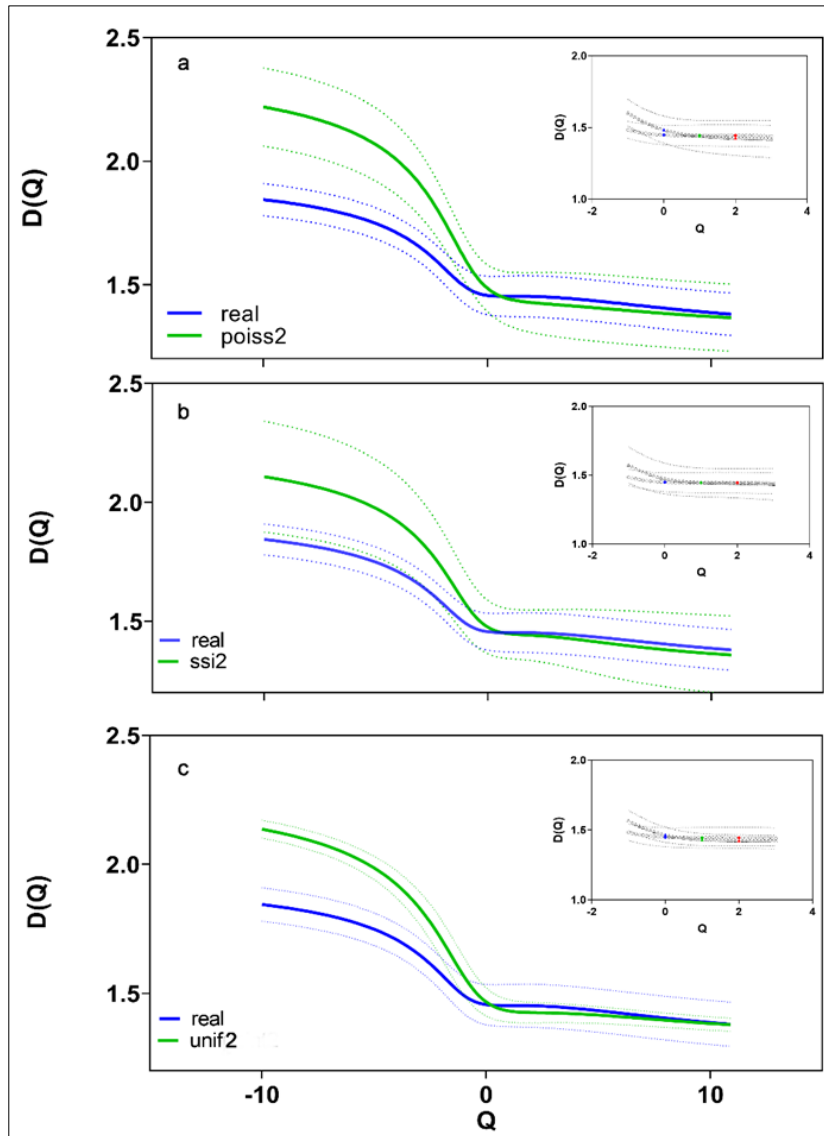
Figure 11 Graphs of the generalized dimension D(Q) as a function of Q. Q values are represented on the X axis, and D(Q) is on the Y axis. a: D(Q) obtained for the cholinergic innervation of the testicular albuginea of the rat (real data) is compared with D(Q) for the poiss 2 network; b: D(Q) of the real data is compared to D(Q) for the ssi 2 network; c: D(Q) of the real data is compared to D(Q) for the unif 2 network. All these networks have been generated by using a tessellation matrix. The insets of each graph show the section of the curve between Q = 0 and Q = 2 to show the dimension of capacity Q_0 (blue), information Q_1 (green), and correlation Q_2 (red). The dotted lines for each curve express the 95% confidence intervals (CI)
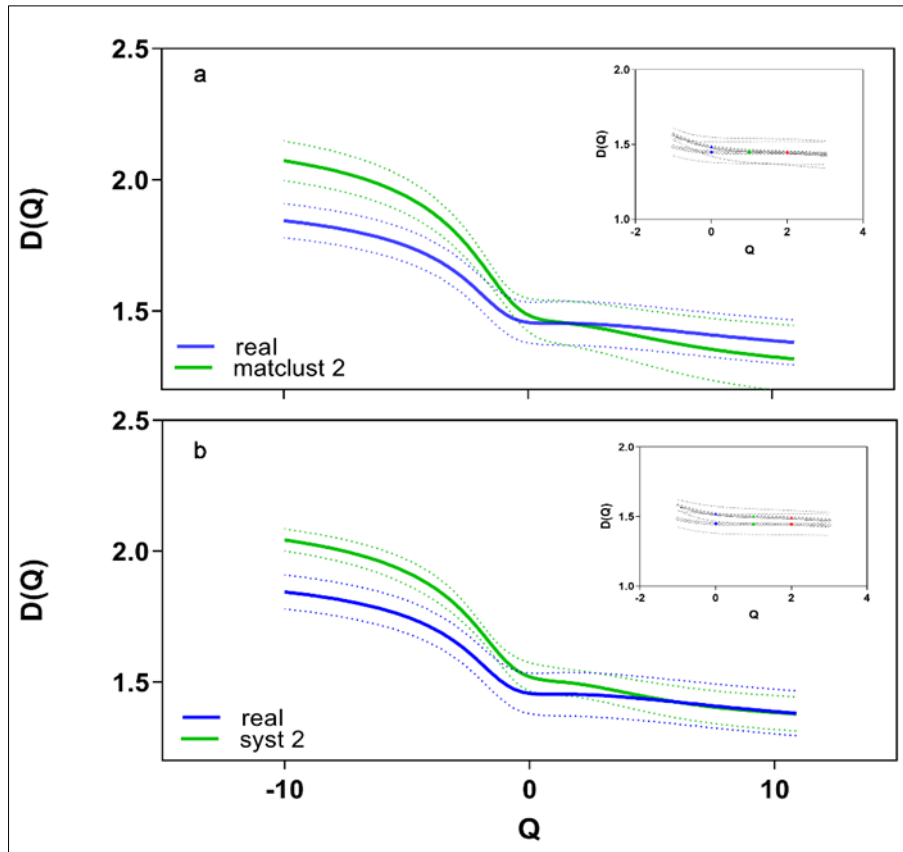
Figure 12 Graphs of the generalized dimension D(Q) as a function of Q. Q values are represented on the X axis, and D(Q) is on the Y axis. a: D(Q) obtained for the cholinergic innervation of the testicular albuginea of the rat (real data) is compared with D(Q) for the matclust 2 network; b: D(Q) of the real data is compared to D(Q) for the syst 2 network. All these networks have been generated by using a tessellation matrix. The insets of each graph show the section of the curve between Q = 0 and Q = 2 to show the dimension of capacity Q_0 (blue), information Q_1 (green), and correlation Q_2 (red). The dotted lines for each curve express the 95% confidence intervals (CI)

For the real data, no significant differences have been observed between the capacity dimension ($D_0 = 1.449 \pm 0.055$), the information dimension ($D_1 = 1.446 \pm 0.059$), and the correlation dimension ($D_2 = 1.445 \pm 0.060$). When D_0 and D_1 of the real data are compared with the same dimensions of the simulated data, it is observed that in the case of the simulations generated from a binary matrix, D_0 and D_1 of the real data are significantly smaller than in the case of the simulations (Figure 13 a,b), while when real D_0 and D_1 are compared with the corresponding dimensions of the simulations generated by a tessellation matrix, there are no significant differences (Figure 13 c,d).
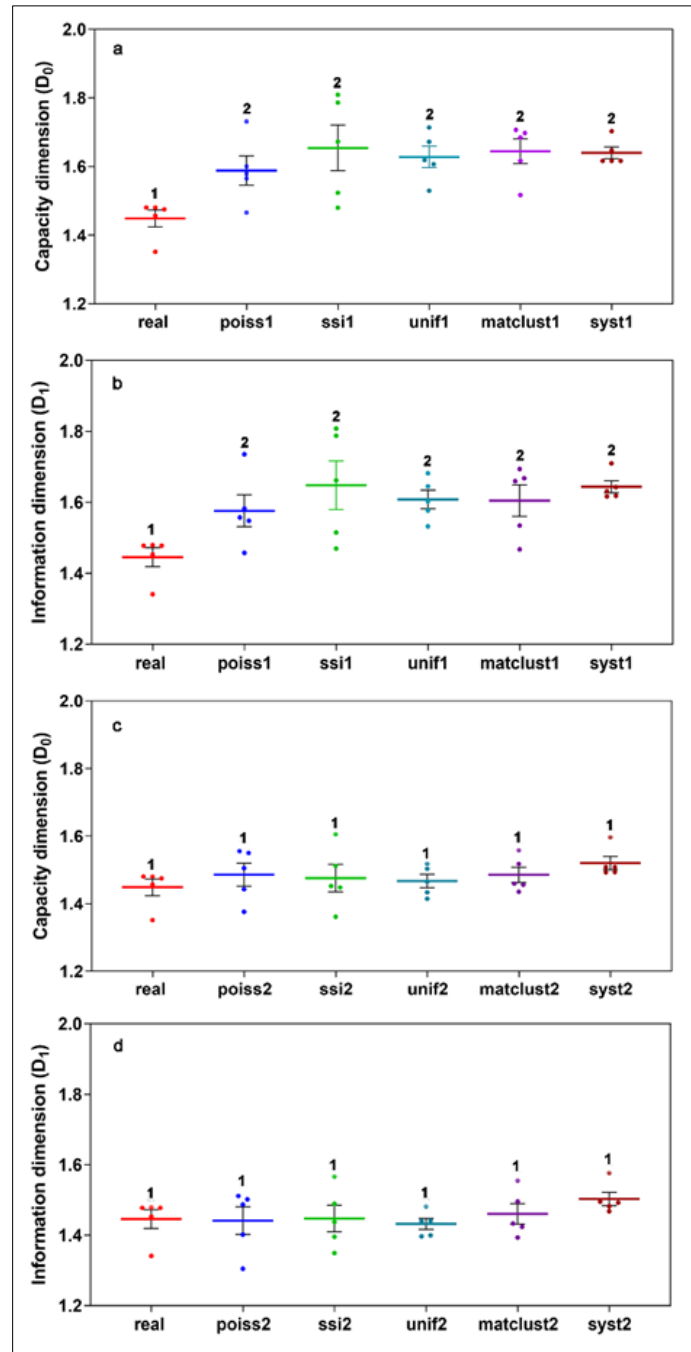
Figure 13 a Scatter dots of the real data's capacity dimension (Q_0) compared to the network models obtained from a binary matrix. b: Scatter dots of the information dimension (Q_1) of the real data compared to the network models obtained from a binary matrix. c: Scatter dots of the real data's capacity dimension (Q_0) compared to the network models obtained from a tessellation matrix. d: Scatter dots of the information dimension (Q_1) of the real data compared to the network models obtained from a tessellation matrix. In all the images, the dots indicate the individual cases of each group, the horizontal lines represent the mean, and the error bars indicate the SEM. Numbers placed above each error bar show significance: Error bars affected by different numbers indicate significant differences of simulated data compared to real data. Error bars affected by equal numbers indicate non-significant differences between those groups

The results are similar for the case of D_2, except that D_2 of the real data does not show significant differences with D_2 of the simulated network poiss1 (Figure 14).
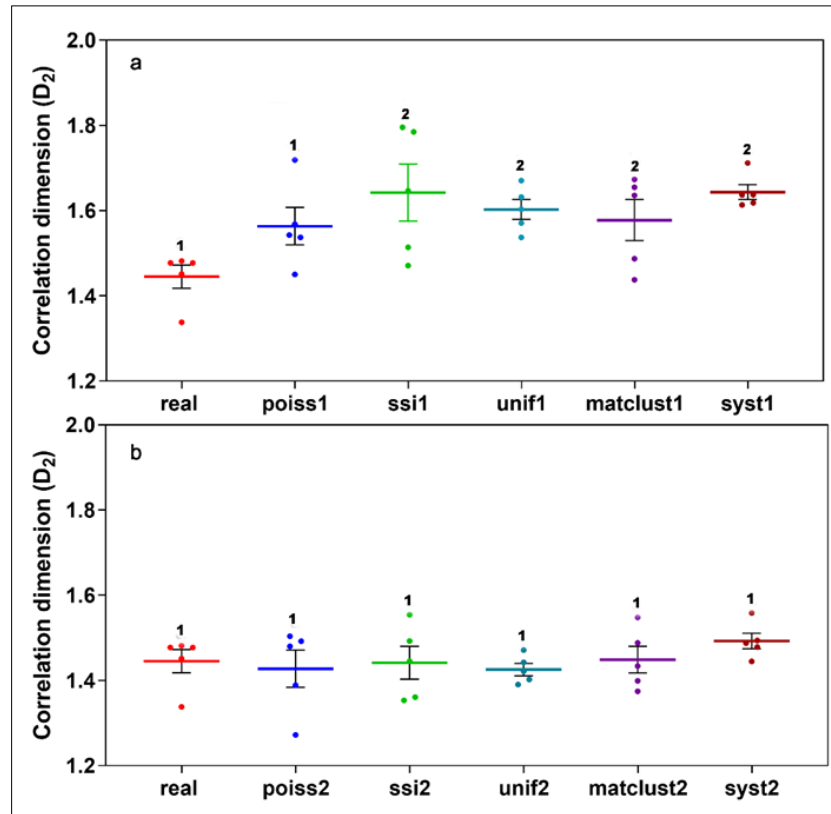
Figure 14 a Scatter dots of the correlation dimension (Q2) of the real data compared to the network models obtained from a binary matrix. b: Scatter dots of the correlation dimension (Q2) of the real data compared to the network models obtained from a tessellation matrix. In both images, the dots indicate the individual cases of each group, the horizontal lines represent the mean, and the error bars indicate the SEM. Numbers placed above each error bar show significance: Error bars affected by different numbers indicate significant differences of simulated data compared to real data. Error bars affected by equal numbers indicate non-significant differences between those groups

4   Discussion

Mathematical modeling of real complex networks aims to characterize their architecture and decipher their underlying principles. Self-repeating patterns and multifractality exist in many real-world complex systems such as the brain, genetics, geoscience, and social networks [44], in the same way as for other biological structures and systems [7, 45-47], the cholinergic nerve plexuses of the testicular albuginea of the rat show a multifractal behavior, as evidenced by the curve of the $f(\alpha)$ spectrum that adopts a humped morphology with the branch corresponding to the range of values $Q \leq 0$ (showing the weak singularities) more open than the branch corresponding to the strong singularities ($Q \geq 0$) [7]. The spectrum $f(\alpha)$ of the real data is similar in morphology to those obtained in the various simulation models used; however, there are apparent differences depending on the type of model used: in all the models obtained from a binary connection matrix, there is no overlapping of the simulated spectra with the real one and the divergence of the real data, being significantly higher than the ρ of the simulations, suggests that the multifractality of the real data is greater than that of the simulated networks. However, in the comparison of the real $f(\alpha)$ with the $f(\alpha)$ of the models obtained from a tessellation matrix, a more remarkable similarity of the multifractal scale is observed since the ρ of the real data does not differ significantly from the ρ of the simulated data, this similarity is particularly remarkable when considering the branch of the curve $f(\alpha)$ that manifests strong singularities ($Q \geq 0$) [7]. In general, the $f(\alpha)$ curve of the models obtained from tessellation matrices is more asymmetric than the $f(\alpha)$ of the real data, manifesting this asymmetry at the expense of the branch of the curve that indicates weak singularities ($Q \leq 0$). As in other studies carried out on very diverse objects [7, 48], the curvature and symmetry of the $f(\alpha)$ spectra provide information on the heterogeneity. As reported in the literature [49], the generalized dimension D_Q is defined for all real Q and is a monotone decreasing function of Q. There are lower and upper limiting dimensions $D_{-\infty}$ and $D_{+\infty}$, respectively, which are related to the regions of the set, in which the measure is "most dilute" and "most dense" respectively. The graphs that show the evolution of the generalized fractal dimension (D_Q) indicate that the D_Q values of the real data are above the D_Q values for the simulated data, especially in the range of weak singularities ($Q \geq 0$). For values in the range of strong singularities ($Q \leq 0$), overlapping

the real D_Q with the simulated ones is more relevant for the models generated by a tessellation matrix. All of the above agrees with what was observed for the multifractal spectrum $f(\alpha)$. The dimensions of capacity (D_0), information (D_1), and correlation (D_2) that are considered particular cases of the continuous spectrum of generalized dimensions (D_Q) [50] have similar values for the real data and also coincide with the corresponding ones of the simulations generated by a tessellation matrix, this corroborates what is suggested by the multifractal spectra, in the sense that the network models generated by this type of matrices have a multifractal scaling more similar to that of the real data than the models originated by a binary matrix. In multifractals, it is described that D_0, D_1, and D_2 differ from each other, with decreasing values from D_0 to D_2 [49, 50], however in the present study, although this order is observed from highest to lowest between D_0 and D_2, the differences are not significant, in this sense, and although the scaling pattern for both $f(\alpha)$ and D_Q seems to be multifractal, the absence of significant differences between D_0, D_1, and D_2 could suggest that the scaling of the real data would be monofractal [49]. Voronoi tessellations models [25] have been used to simulate various biological structures such as pulmonary acini [27], nerve cell patterns [28], distribution of normal and pathological renal glomeruli [26], in the present work it is observed that the multifractal structure of the cholinergic nerve plexuses of the testicular albuginea of the rat is similar to that observed in network models built from a tessellation matrix, regardless of the type of distribution of points used to build the model.

5   Conclusion

In summary, we can conclude that: a) The cholinergic nerve plexuses of the testicular albuginea of the rat show a multifractal behavior; b) The multifractality of the real data is greater than that of the simulated networks; c) However, Voronoi tessellations models show a greater similarity of the multifractal scale with the real data in comparison with those generated by a binary matrix.

Compliance with ethical standards

Disclosure of conflict of interest

No conflict of interest to be disclosed.

Statement of ethical approval

The animals were manipulated under the bioethical standards of international organizations (WMA Statement on Animal Use in Biomedical Research), European Union guidelines, and Spanish State and Local regulations for the use of animals in research, and approved by the Ethical and Animal Studies Committee of the Autonomous University of Madrid.

References

[1]   Risley PL and Skrepetos CN. Histochemical Distribution of Cholinesterases in the Testis, Epididymis, and Vas Deferens of the Rat. Anat Rec. 1964, 148:231-49. https://doi.org/10.1002/ar.1091480213

[2]   Reoyo Jiménez A. Estudio de la inervación aminérgica y colinérgica de la albugínea testicular de la rata en relación con la presencia de células contráctiles. Tesis Doctoral. Madrid: Universidad Autónoma. Facultad de Medicina, Departamento de Morfología. 1988. 1-148pp.

[3]   Santamaria L and Ingelmo I. Length measurement of cholinergic innervation in the tunica albuginea of rat testis. [Internet]. [Cited: 2023 Octub 19]. DOI: bioRxiv preprint https://doi.org/10.1101/2023.10.16.561716. Available from: https://www.biorxiv.org/content/10.1101/2023.10.16.561716v1.full.pdf

[4]   Landini G and Rippin JW. Fractal dimensions of the epithelial-connective tissue interfaces in premalignant and malignant epithelial lesions of the floor of the mouth. Anal Quant Cytol Histol. 1993, 15(2):144-9.

[5]   Losa GA and Nonnenmacher TF. Self-similarity and fractal irregularity in pathologic tissues. Mod Pathol. 1996, 9(3):174-82.

[6]   Sedivy R and Windischberger C. Fractal analysis of a breast carcinoma--presentation of a modern morphometric method. Wien Med Wochenschr. 1998, 148(14):335-7.

[7] Sijilmassi O, López Alonso JM, Del Río Sevilla A, Barrio Asensio MC. Multifractal analysis of embryonic eye structures from female mice with dietary folic acid deficiency. Part I: Fractal dimension, lacunarity, divergence, and multifractal spectrum. Chaos Solitons Fractals. 2020, 138(Article 109885):1-13.

[8] Ivanov PC, Amaral LA, Goldberger AL, Havlin S, Rosenblum MG, Struzik ZR, Stanley HE. Multifractality in human heartbeat dynamics. Nature. 1999, 399(6735):461-5. https://doi.org/10.1038/20924

[9] Reljin IS and Reljin BD. Fractal geometry and multifractals in analyzing and processing medical data and images. Archive of Oncology. 2002, 10(4):283-93. https://doi.org/10.2298/AOO0204283R

[10] Mandelbrot B. Intermittent turbulence in self-similar cascades: Divergence of high moments and dimension of the carrier. Journal of Fluid Mechanics. 1974, 62(2):331-58. https://doi.org/10.1017/S0022112074000711

[11] Mandelbrot BB. La geometría fractal de la naturaleza. Barcelona. TusQuets Editores, S.A. 1997.

[12] Takayasu H. Fractals in the Physical Sciences. Manchester, New York. Manchester University Press. 1990.

[13] Abarbanel HDI. Analysis of observed chaotic data. New York. Springer Verlag. 1996.

[14] Ruiz De las Heras J. Aplicación de herramientas estereológicas y de cuantificación no lineal al estudio de la distribución, isotropía y tamaño del lecho microvascular en próstata normal y patológica. Tesis Doctoral. Madrid: Universidad Autónoma de Madrid. Facultad de Medicina, Departamento de Cirugía. 2010. 263pp.

[15] Skinner JE, Molnar M, Vybiral T, Mitra M. Application of chaos theory to biology and medicine. Integr Physiol Behav Sci. 1992, 27(1):39-53. https://doi.org/10.1007/BF02691091

[16] Theiler J. Estimating the fractal dimension of chaotic time series. The Lincoln Laboratory Journal. 1990, 3(1):63-85.

[17] Mattfeldt T. Nonlinear deterministic analysis of tissue texture: a stereological study on mastopathic and mammary cancer tissue using chaos theory. J Microsc. 1997, 185(Pt 1):47-66. https://doi.org/10.1046/j.1365-2818.1997.1440701.x

[18] Grassberger P and Procaccia I. Characterization of strange attractors. Physical Review Letters. 1983, 50(5):346-9.

[19] Grassberger P and Procaccia I. Measuring the strangeness of strange attractors. Physica D: Nonlinear Phenomena. 1983, 9(1-2):189-208. https://doi.org/10.1016/0167-2789(83)90298-1

[20] Grassberger P and Procaccia I. Dimensions and entropies of strange attractors from fluctuating dynamics approach. Physica D: Nonlinear Phenomena. 1984, 13(1-2):34-54. https://doi.org/10.1016/0167-2789(84)90269-0.

[21] Hentschel HGE and Procaccia I. The infinite number of generalized dimensions of fractals and strange attractors. Physica D: Nonlinear Phenomena. 1983, 8(3):435-44. https://doi.org/10.1016/0167-2789(83)90235-X

[22] Halsey TC, Jensen MH, Kadanoff LP, Procaccia II, Shraiman BI. Fractal measures and their singularities: The characterization of strange sets. Phys Rev A Gen Phys. 1986, 33(2):1141-51. https://doi.org/10.1103/physreva.33.1141

[23] Sisworo S. On Hölder Exponents. Matematika & Sains. 1999, 4(3):244-9.

[24] West BJ. Fractal physiology and the fractional calculus: a perspective. Front Physiol. 2010, 1(article 12):1-17. https://doi.org/10.3389/fphys.2010.00012

[25] Bock M, Tyagi AK, Kreft JU, Alt W. Generalized Voronoi tessellation as a model of two-dimensional cell tissue dynamics. Bull Math Biol. 2010, 72(7):1696-731. https://doi.org/10.1007/s11538-009-9498-3

[26] Wong B, Farrell ML, Yang S, Freitas T, Lozanoff S. Tessellation analysis of glomerular spatial arrangement in mice with heritable renal hypoplasia. Anat Rec (Hoboken). 2010, 293(2):280-90. https://doi.org/10.1002/ar.21038

[27] Koshiyama K and Wada S. Mathematical model of a heterogeneous pulmonary acinus structure. Comput Biol Med. 2015, 62:25-32. https://doi.org/10.1016/j.compbiomed.2015.03.032

[28] Eglen SJ, Lofgreen DD, Raven MA, Reese BE. Analysis of spatial relationships in three dimensions: tools for the study of nerve cell patterning. BMC Neurosci. 2008, 9:68. https://doi.org/10.1186/1471-2202-9-68

[29] Nakakita K, Imai H, Kamei I, Naka Y, Nakai K, Itakura T, Komai N. Innervation of the cerebral veins as compared with the cerebral arteries: a histochemical and electron microscopic study. J Cereb Blood Flow Metab. 1983, 3(1):127-32. https://doi.org/10.1038/jcbfm.1983.16

[30] Davis JR, Langford GA, Kirby PJ. The testicular capsule. In: Jhonson AD, Gomes WR and Vandermark NL, (edits). The testis, vol 1: development, anatomy and physiology. New York. Academic Press. 1970. p:281-337.

[31] Karnovsky MJ and Roots L. A "Direct-Coloring" Thiocholine Method for Cholinesterases. J Histochem Cytochem. 1964, 12:219-21. https://doi.org/10.1177/12.3.219

[32] Koelle GB. The elimination of enzymatic diffusion artifacts in the histochemical localization of cholinesterases and a survey of their cellular distributions. J Pharmacol Exp Ther. 1951, 103(2):153-71.

[33] Koelle GB. The histochemical identification of acetylcholinesterase in cholinergic, adrenergic and sensory neurons. J Pharmacol Exp Ther. 1955, 114(2):167-84.

[34] Koelle GB and Friedenwald JA. A histochemical method for localizing cholinesterase activity. Proc Soc Exp Biol Med. 1949, 70(4):617-22. https://doi.org/10.3181/00379727-70-17013

[35] Koelle GB and Gromadzki CG. Comparison of the gold-thiocholine and gold-thiolacetic acid methods for the histochemical localization of acetylcholinesterase and cholinesterases. J Histochem Cytochem. 1966, 14(6):443-54. https://doi.org/10.1177/14.6.443

[36] Koelle WA and Koelle GB. The localization of external or functional acetylcholinesterase at the synapses of autonomic ganglia. J Pharmacol Exp Ther. 1959, 126(1):1-8.

[37] El-Badawi A and Schenk EA. The distribution of cholinergic and adrenergic nerves in the mammalian epididymis: a comparative histochemical study. Am J Anat. 1967, 121(1):1-14. https://doi.org/10.1002/aja.1001210102

[38] Santamaria L, Reoyo A, Regadera J, Paniagua R. Histochemistry and ultrastructure of nerve fibres and contractile cells in the tunica albuginea of the rat testis. Acta Anat (Basel). 1990, 139(2):126-33. https://doi.org/10.1159/000146988

[39] Waiskopf N and Soreq H. Cholinesterase Inhibitors: From Molecular Mechanisms of Action to Current and Future Prospects. In: Gupta RC, (edit). Handbook of Toxicology of Chemical Warfare Agents. 2ed. Londres. Nueva York. Academic Press. Elsevier. 2015. p:761-78.

[40] Rasband WS and Bright DS. NIH Image: A Public Domain Image Processing Program for the Macintosh. Microbeam Analysis Soc Jour. 1995, 4:137-49.

[41] Baddeley A and Turner R. Spatstat: An R Package for Analyzing Spatial Point Patterns. Journal of Statistical Software. 2005, 12(6):1-42. https://doi.org/10.18637/jss.v012.i06

[42] Baddeley A and Turner R. Modelling spatial point patterns in R. In: Baddeley A, Gregori P, Mateu J, Stoica R and Stoyan D, (edits). Case Studies in Spatial Point Pattern Modelling, Lecture Notes in Statistics, vol 185. New York. Springer-Verlag. 2006. p:23-74.

[43] Delaunay B. "Sur la sphère vide. A la mémoire de Georges Voronoï". Bulletin de l'Académie des Sciences de l'URSS. Classe des sciences mathématiques et naturelles. 1934, 6:793–800.

[44] Yang R and Bogdan P. Controlling the Multifractal Generating Measures of Complex Networks. Sci Rep. 2020, 10(1):5541. https://doi.org/10.1038/s41598-020-62380-6

[45] Atupelage C, Nagahashi H, Yamaguchi M, Sakamoto M, Hashiguchi A. Multifractal feature descriptor for histopathology. Anal Cell Pathol (Amst). 2012, 35(2):123-6. https://doi.org/10.3233/ACP-2011-0045

[46] Goldberger AL, Amaral LA, Hausdorff JM, Ivanov P, Peng CK, Stanley HE. Fractal dynamics in physiology: alterations with disease and aging. Proc Natl Acad Sci U S A. 2002, 99(Suppl 1):2466-72. https://doi.org/10.1073/pnas.012579499

[47] Sijilmassi O, López Alonso JM, Del Río Sevilla A, Barrio Asensio MC. Multifractal analysis of embryonic eye tissues from female mice with folic acid deficiency. Part II: Local Connected Fractal Dimension Analysis. Chaos Solitons Fractals. 2020, 138(Article 109887):1-10.

[48] Posadas AN, Giménez D, Quiroz R, Protz R. Multifractal characterization of soil pore systems. Soil Sci Soc Am J. 2003, 67(5):1361-9. https://doi.org/10.2136/sssaj2003.1361

[49] Gammel BM. Kritisches Verhalten und Niederfrequenz-Anomalien beim Quanten-Hall-Effekt. Doktors der Naturwissenschaften (Dr. rer. nat.). München Technischen Universität München, Fakultät für Physik. 1994. 100pp.

[50] Fractal dimension. [Internet]. Wikipedia, the free encyclopedia. (Date of update: 2023 August 30). Cited: 2023 Sept 30. Available from: https://en.wikipedia.org/w/index.php?title=Fractal_dimension&oldid=1172934246.